

Chiral domain wall dynamics in magnetic heterostructures with bulk Dzyaloshinskii-Moriya interactions

Mei Li,¹ Bin Xi,¹ Jie Lu,^{1,*} and Yongjun Liu^{1,†}

¹College of Physics Science and Technology, Yangzhou University, Yangzhou 225002, People's Republic of China
(Dated: July 9, 2021)

In this work, dynamics of chiral domain walls in long and narrow magnetic heterostructures based on non-centrosymmetric chiral magnets with bulk Dzyaloshinskii-Moriya interactions (DMI) and perpendicular magnetic anisotropy is systematically investigated. The driving forces can be out-of-plane magnetic fields and in-plane currents, correspondingly both steady and precessional flows are considered. Their dividing points (the Walker critical field and current density) are obtained as functions of bulk DMI strength (D_b) and the ratio (κ) of total (crystalline plus shape) anisotropy in the hard axis over that in the easy one. When far beyond Walker breakdown, the dependence curve of wall velocity on external in-plane bias field takes parabolic shape around the compensation point where the total in-plane field disappears. The center shift is determined by D_b , κ , and the wall's topological charge, thus can be used to measure the bulk DMI strength in chiral magnets.

I. INTRODUCTION

Magnetic solitons with spatial localization and topological protection have attracted intense attentions in the past decades due to both academic and industrial interests. Recently, discussions about chiral magnetic solitons stabilized by the Dzyaloshinskii-Moriya interaction (DMI) become extraordinarily active. The most common examples are chiral domain walls (DWs)[1–6], skyrmions/antiskyrmions[7–11] and bimerons[12–16], etc. Historically, the bulk DMI (bDMI) was first proposed which should phenomenologically include an odd term of the spatial gradient of magnetization as a result of being an antisymmetric exchange coupling[17]. From the microscopic viewpoint, bDMI comes from the generalization of Anderson's superexchange theory in the presence of spin-orbit coupling[18]. Experimentally, it was first proposed to reside in chiral magnets with non-centrosymmetric B20 structure[7, 8, 19, 20]. In addition, the non-collinear magnetic structures observed recently in several Heusler compounds also suggest its possible existence therein[21, 22]. Magnetic heterostructures based on these novel materials with bDMI should open new possibility of future spintronics devices with chiral magnetic solitons serving as carriers of information recording and transmission.

In many proposed experiments, magnetic heterostructures are prepared on heavy-metal substrates[23–37]. In these setups, the interfacial DMI (iDMI), spin Hall and Rashba spin-orbit torques emerge thus complicatedly manipulate the motion of chiral DWs in the primary magnetic layer under external currents[33–38]. To explore the effects of pure bDMI on chiral-DW dynamics, in this work we focus on long and narrow magnetic heterostructures in which chiral magnets with perpendicular magnetic anisotropy (PMA) are sandwiched between normal insulating substrates and cplayers. Once nucleated, chiral DWs can be driven to move longitudinally by either out-of-plane magnetic fields or in-plane currents. In principle, both steady and precessional flows can emerge. However their dividing point, the Walker limit, will be manipulated by the bDMI subtly. When far beyond the

Walker breakdown, the dependence of wall velocity on in-plane magnetic bias fields is explored. The resulting curves take parabolic shapes around the compensation point where the total (external plus internal) in-plane field disappears. Accordingly, the bDMI strength can be obtained directly from the center shifts of these curves.

The rest of this paper is organized as follows. In Sec. II the system set up and its modelization are briefly introduced. Also, the Lagrangian-based collective coordinate model adopted is presented. Then the chirality of static walls is investigated in Sec. III. After that, the field-driven and current-driven dynamics of chiral DWs are systematically studied in Sec. IV and V, respectively. Finally, concluding remarks are provided in the last section.

II. MODEL AND PREPARATION

Generally, the magnetic free-energy density \mathcal{E}_0 of the chiral magnet in a heterostructure (see Fig. 1) includes four parts: the exchange part $\mathcal{E}_{\text{ex}} = A(\nabla \mathbf{m})^2$ (A and \mathbf{m} being the exchange stiffness and magnetization unit vector, respectively), the Zeeman part $\mathcal{E}_Z = -\mu_0 M_s \mathbf{m} \cdot \mathbf{H}_a$ with the total external field $\mathbf{H}_a = \mathbf{H}_z + \mathbf{H}_\perp$ and the saturation magnetization M_s , the anisotropy part $\mathcal{E}_{\text{ani}} = (\mu_0 M_s^2 / 2)(-k_E m_z^2 + k_H m_y^2)$ where k_E (k_H) is the total (crystalline plus shape) anisotropy coefficient in easy (hard) axis (in this work we consider PMA, which is the most common in chiral magnets), and the bDMI contribution $\mathcal{E}_b = D_b \mathbf{m}(\mathbf{r}) \cdot [\nabla \times \mathbf{m}(\mathbf{r})]$ with D_b being the bDMI strength[39]. The corresponding bDMI-induced effective field then reads $\mathbf{H}_b(\mathbf{r}) = -2D_b(\nabla \times \mathbf{m})/(\mu_0 M_s)$.

Under out-of-plane magnetic fields and in-plane currents, the Lagrangian \mathcal{L} of this chiral magnet is

$$\frac{\mathcal{L}}{\mu_0 M_s^2} = -\frac{\cos \theta}{\gamma M_s} \frac{\partial \phi}{\partial t} - \frac{B_J \phi}{\gamma M_s} \frac{\partial \cos \theta}{\partial (\hat{\mathbf{J}} \cdot \mathbf{r})} - \frac{\mathcal{E}_0}{\mu_0 M_s^2}, \quad (1)$$

with the dissipative functional

$$\frac{\mathcal{F}}{\mu_0 M_s^2} = \frac{\alpha}{2\gamma M_s} \left\{ \left[\frac{\partial}{\partial t} - \frac{\beta B_J}{\alpha} \frac{\partial}{\partial (\hat{\mathbf{J}} \cdot \mathbf{r})} \right] \mathbf{m} \right\}^2 \quad (2)$$

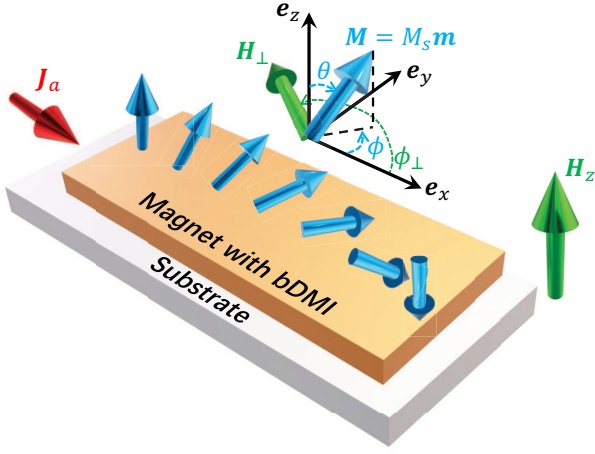


FIG. 1. (Color online) Sketch of a narrow-strip-shaped heterostructure in which a magnet with bDMI and PMA is prepared on a non-magnetic substrate. The magnetization $\mathbf{M} = M_s \mathbf{m}$ can be fully described by its polar and azimuthal angles (θ and ϕ). An “ $\uparrow\downarrow$ ” wall is driven to move in x -direction by either an external in-plane current density \mathbf{J}_a or an out-of-plane field \mathbf{H}_z . In the meantime, an in-plane bias field, $\mathbf{H}_\perp = H_\perp (\cos \phi_\perp \mathbf{e}_x + \sin \phi_\perp \mathbf{e}_y)$, is applied to manipulate the wall’s behavior.

describing the various damping processes[40–45]. Here $\theta(\mathbf{r}, t)$ and $\phi(\mathbf{r}, t)$ are the polar and azimuthal angles of $\mathbf{m}(\mathbf{r}, t)$, respectively. α is the damping constant and β is the nonadiabatic spin-transfer torque (STT) coefficient. $\gamma = \mu_0 \gamma_e$ with μ_0 and γ_e being the vacuum permeability and electron gyromagnetic ratio, respectively. $B_J = \mu_B P j_a / (e M_s)$, in which μ_B is the Bohr magneton and $e (> 0)$ is the absolute electron charge. j_a (with unit vector $\hat{\mathbf{J}}$) is the current density flowing longitudinally through the chiral magnet with polarization P .

The magnetization dynamics of the chiral magnet is described by the generalized Lagrangian equation,

$$\frac{d}{dt} \left(\frac{\delta \mathcal{L}}{\delta \dot{X}} \right) - \frac{\delta \mathcal{L}}{\delta X} + \frac{\delta \mathcal{F}}{\delta \dot{X}} = 0, \quad (3)$$

where an overdot means $\partial/\partial t$ and X is any related coordinate. To explore collective behaviors, we use the Lagrangian-based collective coordinate model which needs preset ansatz of DWs. For long and narrow heterostructures, we take the quasi one dimensional (1D) Walker ansatz[46, 47]

$$\ln \tan \frac{\vartheta}{2} = \eta \frac{x - q(t)}{\Delta}, \quad \phi = \varphi(t) \quad (4)$$

$$\frac{(E_0)_{\min}}{\pi S D_0} = \begin{cases} \sqrt{\left(1 + \frac{1}{\kappa}\right) \frac{1}{\kappa} - \left(\frac{D_b}{D_0}\right)^2} \frac{1}{\kappa} & \text{at } \sin \varphi_0 = -\eta \operatorname{sgn}(D_b) \sqrt{\frac{(D_b/D_0)^2}{(1+\kappa) - \kappa(D_b/D_0)^2}} \text{ for } |D_b| \leq D_0, \\ \left(1 + \frac{1}{\kappa}\right) - \frac{|D_b|}{D_0} & \text{at } \sin \varphi_0 = -\eta \operatorname{sgn}(D_b) \text{ for } |D_b| > D_0, \end{cases} \quad (6)$$

with $D_0 \equiv (2M_s k_H / \pi) \sqrt{2A \mu_0 / (k_E + k_H)}$ and “sgn” being the

sign function. This means that for finite bDMI ($|D_b| \leq D_0$),

in which q , Δ , and φ are wall center position, wall width and in-plane magnetization angle, respectively. $\eta = +1(-1)$ is the topological wall charge which corresponds to “ $\uparrow\downarrow$ ($\downarrow\uparrow$)” wall. For narrow-strip geometry as shown in Fig. 1, the \mathbf{e}_x and \mathbf{e}_y axes respectively indicate the “longitudinal (L)” and “transverse (T)” directions. For this quasi one-dimensional system, the in-plane component of the effective field from bDMI becomes $\mathbf{H}_b(x) = 2D_b (\nabla_x m_z) \mathbf{e}_y / (\mu_0 M_s)$. Clearly, \mathbf{H}_b has transverse component proportional to $\nabla_x m_z$, which is reversed under wall charge reversal $\eta \rightarrow -\eta$. By setting $X = q$, φ , Δ and integrating the resulting equations along longitudinal direction ($\int_{-\infty}^{+\infty} dx$), the following closed dynamical equation set is obtained,

$$\begin{aligned} (1 + \alpha^2) \dot{\varphi} &= \gamma H_z + (\alpha - \beta) \frac{\eta B_J}{\Delta} - \frac{\alpha \pi \gamma}{2} \left[\frac{k_H M_s}{\pi} \sin 2\varphi \right. \\ &\quad \left. + H_\perp \sin(\varphi - \phi_\perp) + \frac{\eta D_b \cos \varphi}{\mu_0 M_s \Delta} \right], \\ \dot{q} &= -\frac{\eta \Delta}{\alpha} \dot{\varphi} + \frac{\eta \Delta \gamma}{\alpha} H_z - \frac{\beta}{\alpha} B_J, \\ \frac{\alpha \pi \dot{\Delta}}{6 \gamma_0 \Delta} &= \frac{2A}{\pi \mu_0 M_s \Delta^2} - \frac{M_s}{\pi} (k_E + k_H \sin^2 \varphi) \\ &\quad + H_\perp \cos(\varphi - \phi_\perp). \end{aligned} \quad (5)$$

These are all we need to proceed our investigation.

III. CHIRALITY OF STATIC WALLS

As the first step, the chirality of static walls selected by bDMI is explored. When $H_z = 0$ and $j_a = 0$, the wall keeps static. Under the Walker profile and in the absence of in-plane bias fields, the total magnetic energy $E_0/S = \int_{-\infty}^{+\infty} \mathcal{E}_0[\mathbf{M}] dx = 2A/\Delta + \mu_0 M_s^2 \Delta (k_E + k_H \sin^2 \varphi) + \eta \pi D_b \sin \varphi$, in which S is the cross-sectional area of the chiral magnet. For static walls, the last equation in Eq. (5) provides $\Delta = \Delta_0 (1 + \kappa \sin^2 \varphi)^{-1/2}$ with $\Delta_0 = \sqrt{2A / (\mu_0 k_E M_s^2)}$ and $\kappa = k_H / k_E$. Therefore, one has $E_0/S = 2[2A \mu_0 M_s^2 (k_E + k_H \sin^2 \varphi)]^{1/2} + \eta \pi D_b \sin \varphi$. Obviously when bDMI is absent, either $\varphi = 0$ or $\varphi = \pi$ provides the minimum of E_0 thus the wall takes Néel-type profile and no chirality is preferred. However, as D_b appears, the minimization operation of E_0/S provides,

sign function. This means that for finite bDMI ($|D_b| \leq D_0$),

the wall profile is a mixture of Néel and Bloch types thus shows certain chirality preference through non-zero $\langle m_y \rangle$. While for sufficiently large bDMI ($|D_b| > D_0$), chiral Bloch walls emerge. This process is shown in Fig. 2 where $\eta = +1$ and $D_b < 0$ are taken as an example.

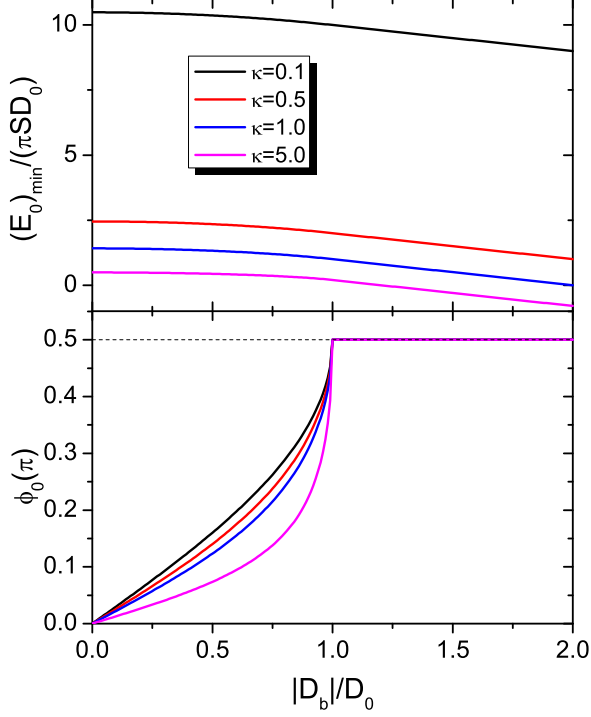


FIG. 2. (Color online) Evolution of (a) minimum total magnetic energy and (b) the corresponding in-plane angle of chiral DWs as bDMI increases. Four typical “hard-easy ratio” κ are presented. Obviously for a given κ , there exists a critical bDMI strength D_0 . When $|D_b| < D_0$ ($\geq D_0$), the wall shows partial (full) chirality.

When finite out-of-plane fields and/or in-plane currents are applied, Eq. (5) implies that there should be two dynamical modes: the steady-flow mode for small driving factors and the precessional-flow mode for sufficiently large external stimuli. The dividing point is the “Walker field” or “Walker current density”, which will be manipulated by the bDMI. In the following two sections, field- and current-driven dynamics of these chiral DWs will be respectively investigated.

IV. FIELD-DRIVEN DYNAMICS

In this section, we focus on the chiral DWs dynamics under pure out-of-plane driving field $\mathbf{H}_z = H_z \mathbf{e}_z$. First in the absence of \mathbf{H}_\perp , the effects of bDMI on both Walker field and high-field wall behaviors are investigated. Further manipulations of in-plane bias fields to chiral walls’ velocity under high H_z are

then analyzed which provides applicable procedure of measuring the bDMI strength D_b .

IV.A Enlarged Walker field

First we define several quantities for convenience. They are: the anisotropy field in hard axis $H_K = k_H M_s$, the original Walker field $H_W^0 = \alpha H_K / 2$, the bDMI effective field strength $H_b^0 = D_b / (\mu_0 M_s \Delta_0)$, and the dimensionless coefficient $b = \eta \pi H_b^0 / H_K$. In the absence of \mathbf{H}_\perp and j_a , the rigid-flow mode requires $\dot{\varphi} = 0$ and $\dot{\Delta} = 0$ which leads to

$$\frac{H_z}{H_W^0} = f(\varphi) \equiv b \cos \varphi \sqrt{1 + \kappa \sin^2 \varphi} + \sin 2\varphi. \quad (7)$$

For fixed b and κ , once the maximum absolute value of the function f , i.e. $|f(\varphi)|_{\max}$, is found for $\varphi \in [0, 2\pi)$, the new Walker field then reads $H_W = H_W^0 |f(\varphi)|_{\max}$.

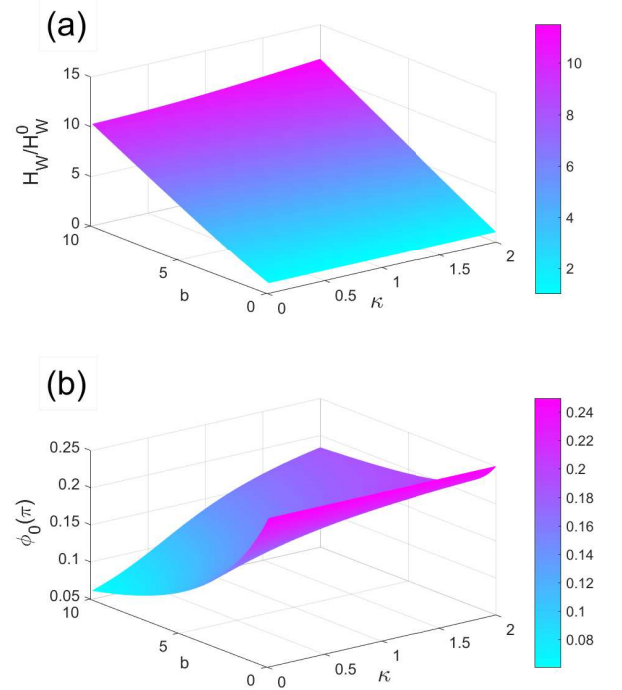


FIG. 3. (Color online) (a) The new Walker field H_W in the presence of bDMI and (b) the corresponding in-plane angle at which H_W is achieved as functions of the bDMI effective field strength ($b = \eta \pi H_b^0 / H_K$) and “hard-easy ratio” κ . The data are calculated based on the results in Appendix A.

Before presenting the detailed results, several points need to be clarified: (i) the sign of b does not affect $|f(\varphi)|_{\max}$ since we always have $f(b, \varphi) = f(-b, \varphi + \pi)$. Therefore without loss of generality, we set $b > 0$. (ii) if κ can be neglected, then after simple algebra we find that at $\sin \varphi = (-b + \sqrt{b^2 + 32})/8$ the function f reaches its maximum absolute value $|f(\varphi, \kappa = 0)|_{\max} = \sqrt{(-b^4 + 80b^2 + 128) + b(b^2 + 32)^{3/2}}/8\sqrt{2}$, which

recovers the result in one of our recent works[6]. However, in real magnetic heterostructures, κ is generally the order of 1. After systematic calculus, the explicit form of $|f(\varphi)|_{\max}$ can be obtained analytically (see Appendix A). Based on it, the enlarged Walker field H_W (in the unit of H_W^0) and the corresponding in-plane angle φ_0 where H_W is achieved are calculated and plotted in Fig. 3(a) and 3(b), respectively. As bDMI gradually increases, the Walker field is enlarged and its location, φ_0 , decreases from $\pi/4$ to 0. Obviously, the “hard-easy ratio” κ hardly affects H_W/H_W^0 however it strongly manipulates its location φ_0 . When $\kappa \gg 1$ the location of Walker field is nearly unchanged. This can be easily understood from Eq. (7) since now one has $f(\varphi) \sim (b\sqrt{\kappa}/2 + 1)\sin 2\varphi$, which achieves its maximum at $\varphi = \pi/4$.

For $|H_z| < H_W$, one should first numerically solve Eq. (7) to obtain the in-plane angle $\varphi(H_z)$ thus the wall width $\Delta = \Delta_0(1 + \kappa \sin^2 \varphi)^{-1/2}$. Then the wall velocity reads $\dot{q} = \eta \Delta \gamma H_z / \alpha$. In particular, given a certain chiral magnet with fixed shape (thus fixed H_b^0 and H_K): (a) for a given wall topological charge η , when $\mathbf{H}_z \rightarrow -\mathbf{H}_z$, one has $\varphi(H_z) \rightarrow \pi - \varphi(H_z)$ leading to unchanged wall width thus opposite wall velocity; (b) for a given \mathbf{H}_z , the $\eta \rightarrow -\eta$ operation results in $\varphi(H_z) \rightarrow \pi + \varphi(H_z)$. Therefore the wall width is also unchanged and eventually wall velocity is reversed.

IV.B $\langle \dot{q} \rangle$ under $|H_z| \gg H_W$

When $|H_z|$ exceeds H_W , the Walker breakdown takes place and the wall falls into precessional-flow mode. Generally the breathing wall width ($\dot{\Delta} \neq 0$) has no explicit expression. In the simplest approximation, one can still take $\Delta = \Delta_0(1 + \kappa \sin^2 \varphi)^{-1/2}$. By integrating the first equation in Eq. (5) in a full circle, the precessional period T_0 is obtained as

$$\bar{\gamma} T_0 = \int_0^{2\pi} \frac{d\varphi / \sqrt{1 + \kappa \sin^2 \varphi}}{\frac{H_z - H_W^0 \sin 2\varphi}{\sqrt{1 + \kappa \sin^2 \varphi}} - \frac{\eta \alpha \pi}{2} H_b^0 \cos \varphi}, \quad (8)$$

where $\bar{\gamma} \equiv \gamma / (1 + \alpha^2)$ and holds throughout this work. When bDMI is absent, the integration can be easily calculated. As bDMI emerges, the situation becomes complicated. Generally, Eq. (8) has no explicit form. However, in the high-field limit in which $|H_z| \gg \alpha |H_b^0| (H_W^0)$, by using the approximation $(1 - \varepsilon)^{-1} \approx 1 + \varepsilon + \varepsilon^2$, Eq. (8) gives

$$T_0 \approx \frac{2\pi}{\bar{\gamma} H_z} \left[1 + \frac{\alpha^2 \pi^2}{8} \left(1 + \frac{\kappa}{4} \right) \left(\frac{H_b^0}{H_z} \right)^2 + \frac{\alpha^2}{8} \left(\frac{H_K}{H_z} \right)^2 \right]. \quad (9)$$

Therefore the time-averaged wall velocity is

$$\langle \dot{q} \rangle_0 = \eta \alpha \Delta_0 \bar{\gamma} H_z \frac{K_0}{2\pi} \left[1 + \frac{\pi^2}{8} \left(1 + \frac{\kappa}{4} \right) \left(\frac{H_b^0}{H_z} \right)^2 + \frac{1}{8} \left(\frac{H_K}{H_z} \right)^2 \right], \quad (10)$$

in which K_0 is defined in Eq. (B1). If the velocity dependence on H_z is the main concern, interestingly Eq. (10) can

be reorganized as $c(H_z - H_0)^2 / H_z + d / H_z$, which is exactly the same as Eq. (9) of our early work in Ref. [48]. Once again, the correctness of our original roadmap on field-driven DW dynamics is verified. Alternatively, when we focus on the manipulation of bDMI on walls’ drifting velocity, a parabolic $\langle \dot{q} \rangle_0 \sim H_b^0$ relationship emerges which is similar to Eq. (9) in Ref. [32]. Note that our result here has two advantages: (a) here the “ $H_W^0 \sin 2\varphi$ ”-term has been preserved thus leading to the $(H_K)^2$ term which is missing in Ref. [32]; (b) the dependence of $\langle \dot{q} \rangle_0$ on the “hard-easy ratio” κ is fully revealed, which has been totally neglected in most existing literatures.

IV.C $\langle \dot{q} \rangle \sim H_\perp$ dependence under high H_z

Next we turn on the in-plane bias field $\mathbf{H}_\perp = H_\perp (\cos \phi_\perp \mathbf{e}_x + \sin \phi_\perp \mathbf{e}_y)$. Generally the Walker field H_W will be further enlarged due to the “pinning” effect of \mathbf{H}_\perp to the in-plane angle φ , however the explicit form is mathematically hopeless due to the mismatch between the symmetries of quadratic anisotropy and linear Zeeman energies. In this subsection, we focus on $\langle \dot{q} \rangle \sim H_\perp$ dependence under sufficiently large H_z where chiral DWs take precessional motion. Similarly, in the simplest approximation the wall width is expressed as $\Delta = \Delta_0(1 + \kappa \sin^2 \varphi)^{-1/2}$. The period for a full circle is similar with that in Eq. (8) except for an additional $-\frac{\alpha \pi}{2} H_\perp \sin(\varphi - \phi_\perp)$ term to the denominator of integral kernel. In the following we examine two typical cases, namely longitudinal and transverse in-plane bias fields, to see the behaviors of $\langle \dot{q} \rangle \sim H_\perp$ dependence curve.

For longitudinal in-plane bias fields, $H_\perp = H_x$ and $\phi_\perp = 0$. For large enough H_z , similar calculation provides the new period as

$$T_x = T_0 + \frac{2\pi}{\bar{\gamma} H_z} \frac{\alpha^2 \pi^2}{8} \left(\frac{H_x}{H_z} \right)^2, \quad (11)$$

thus leads to a new velocity

$$\langle \dot{q} \rangle [H_x] = \langle \dot{q} \rangle_0 + \eta \alpha \Delta_0 \bar{\gamma} H_z \frac{K_0}{2\pi} \frac{\pi^2}{8} \left(\frac{H_x}{H_z} \right)^2. \quad (12)$$

Obviously, for a fixed H_z this $\langle \dot{q} \rangle \sim H_x$ curve is a parabola going upwards (downwards) with its center locating at $H_x = 0$ for $\eta = +1$ (-1).

Alternatively for transverse in-plane bias fields, $H_\perp = H_y$ and $\phi_\perp = \pi/2$. Similar calculation provides the high- H_z period as

$$T_y = T_0 + \frac{2\pi}{\bar{\gamma} H_z} \frac{\alpha^2 \pi^2}{8} \left[\left(\frac{H_y}{H_z} \right)^2 - \frac{\eta K_0}{8\pi} \left(1 + \frac{\kappa}{4} \right) \frac{H_y}{H_z} \frac{H_b^0}{H_z} \right]. \quad (13)$$

The resulting averaged wall velocity is

$$\langle \dot{q} \rangle [H_y] = \langle \dot{q} \rangle_0 + \eta \alpha \Delta_0 \bar{\gamma} H_z \frac{K_0}{2\pi} \frac{\pi^2}{8} \left[\left(\frac{H_y - \delta H_y}{H_z} \right)^2 - \left(1 + \frac{\kappa}{4} \right)^2 \left(\frac{K_0}{2\pi} \right)^2 \left(\frac{H_b^0}{H_z} \right)^2 \right], \quad (14)$$

with $\delta H_y = \eta \left(1 + \frac{\kappa}{4}\right) \frac{K_0}{2\pi} H_b^0$. Therefore for a fixed H_z and $\eta = +1$ (-1), the $\langle \dot{q} \rangle \sim H_y$ curve becomes a parabola going upwards (downwards) with its center locating at $H_y = \delta H_y$. For a given magnetic heterostructure with chiral-magnet central layer, the “hard-easy ratio” κ can be calculated. For a chiral DW with certain wall charge η , by measuring the $\langle \dot{q} \rangle \sim H_y$ dependence one can extract out the bDMI strength D_b from the location of parabola center.

Note that in our recent work in Ref. [43], we have constructed a general scheme of identifying and quantifying bDMI in magnetic heterostructures via precessional flow of chiral DWs under in-plane transverse bias fields. In that scheme, the linearization of trigonometric functions does not lose too many details of the entire circle since DWs precess almost evenly under large enough out-of-plane driving fields. However the “hard-easy ratio” κ is totally neglected since generally people use the static width Δ_0 instead of the real complicated breathing one. This simplification holds for not too narrow magnetic central layers with strong PMA. However for those with relatively weak PMA and shrinking width, the importance of κ will increase significantly. This effect manifests itself as the additional factor $\left(1 + \frac{\kappa}{4}\right) \frac{K_0}{2\pi}$ in our new δH_y . We will revisit this issue in the discussion section later.

V. CURRENT-DRIVEN DYNAMICS

In this section, we turn to in-plane current-driven dynamics of chiral DWs ($H_z = 0$ and $j_a \neq 0$). Parallel deductions will be performed compared with field-driven case in the above section. Effects of bDMI to both Walker current density and wall behaviors under high currents will be explored.

V.A Enlarged Walker current density

Pioneer works provide us that in the absence of bDMI, the in-plane Walker current density is $j_W^0 = \frac{\Delta_0 \gamma H_W^0 e M_s}{|\alpha - \beta| \mu_B P}$. Without \mathbf{H}_\perp , the existence condition of rigid-flow mode ($\dot{\varphi} = 0$ and $\dot{\Delta} = 0$) turns the first equation in Eq. (5) to

$$\eta \operatorname{sgn}(\alpha - \beta) \frac{j_a}{j_W^0} = g(\varphi) \equiv b \cos \varphi + \frac{\sin 2\varphi}{\sqrt{1 + \kappa \sin^2 \varphi}}. \quad (15)$$

Similarly, for fixed b and κ when the maximum absolute value of the function g , i.e. $|g(\varphi)|_{\max}$, is found for $\varphi \in [0, 2\pi)$, the new Walker current density is then obtained as $j_W = j_W^0 |g(\varphi)|_{\max}$. Also, the sign of b is irrelevant to $|g(\varphi)|_{\max}$ since $g(b, \varphi) = g(-b, \varphi + \pi)$ always holds. Therefore we can set $b > 0$ to make the analysis simple. For neglectable κ , $g(\varphi) \equiv f(\varphi, \kappa = 0)$ thus achieves the same maximum as $|f(\varphi, \kappa = 0)|_{\max}$ at the same location. For finite κ , after defining $x \equiv \sin \varphi$ and introducing a new function $\mathcal{G}(x) \equiv [g(\varphi)]^2$, one thus has $|g(\varphi)|_{\max} = \sqrt{|\mathcal{G}(\varphi)|_{\max}}$. The extremum condition, $d\mathcal{G}/dx = 0$, can be transformed into a quartic equation

of x^2 , whose exact solution is too complicated to write out explicitly. Alternatively, by numerically searching the maximum of $\mathcal{G}(x)$ for $x \in [-1, 1]$, the new Walker current density j_W (in the unit of j_W^0) and the corresponding φ_0 where j_W is reached are depicted in Fig. 4(a) and 4(b), respectively. For fixed κ , along with the increase of bDMI j_W is considerably enlarged and its location φ_0 decreases from $\pi/4$ to 0 since the first term in Eq. (15) becomes dominant. On the other hand, κ hardly changes j_W but strongly affects φ_0 , even when bDMI is small. For fixed bDMI when $\kappa \gg 1$ the location φ_0 rapidly decreases from $\pi/4$ to 0. This comes from the fact that now Eq. (15) provides $g(\varphi) \sim (b + 2/\sqrt{\kappa}) \cos \varphi$ which achieve maximum absolute value at $\varphi_0 = 0$. In summary, the huge difference between Fig. 3(b) and 4(b) comes from the subtle distinction between Eqs. (7) and (15), especially for finite κ .

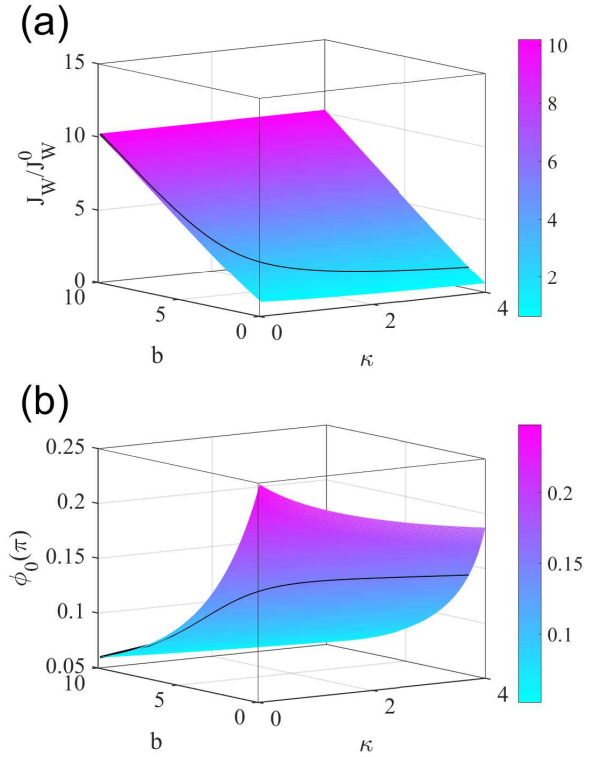


FIG. 4. (Color online) (a) New Walker current density J_W in the unit of $j_W^0 = \frac{\Delta_0 \gamma H_W^0 e M_s}{|\alpha - \beta| \mu_B P}$ and (b) the corresponding in-plane angle under in-plane driving current $j_a \mathbf{e}_x$. All data come from direct numerical searching of the maximum of function $\mathcal{G}(x = \sin \varphi)$ in (b, κ) -space. The solid curve in (b) comes from $\varphi_0 = \arcsin \bar{x}$ in Eq. (16), while that in (a) is $\sqrt{\mathcal{G}(\bar{x})}$.

An interesting special case is “ $b^2 \kappa = 4$ ”, under which the quartic equation of x^2 (coming from $d\mathcal{G}/dx = 0$) is reduced to a cubic equation: “ $\kappa(x^2)^3 + (1 - 2\kappa)(x^2)^2 - (4 + 1/\kappa)x^2 + 1 = 0$ ”. Its solution

$$\bar{x} = \left[\frac{2\kappa - 1}{3\kappa} + \frac{4(1 + \kappa)}{3\kappa} \cos \frac{\theta + \pi}{3} \right]^{\frac{1}{2}}, \quad \theta = \cos^{-1} \frac{11 - \kappa}{1 + \kappa}, \quad (16)$$

corresponds to the maximum of $\mathcal{G}(x)$. The resulting new

Walker current density is $j_W = j_W^0 \sqrt{\mathcal{G}(\bar{x})}$, which has been plotted in Fig. 4(a) by a solid curve. Correspondingly, the in-plane angle $\varphi_0 = \arcsin \bar{x}$ is depicted in Fig. 4(b). The high coincidence between numerics and analytics of this special case provide strong cross-validation for both processing methods. At last for $|j_a| \leq j_W$, the wall takes steady-flow mode with velocity $\dot{q} = -\frac{\beta}{\alpha} B_J$. This means that bDMI does not change the wall's mobility under in-plane currents for steady flows.

V.B $\langle \dot{q} \rangle$ under $|j_a| \gg j_W$

As $|j_a|$ exceeds j_W , steady-flow mode fails and the wall undergoes precessional flow. Under similar approximation and integration over a full circle as in Sec. IV.B, the precession period T'_0 is

$$T'_0 = \frac{1}{\bar{\gamma} H_W^0} \int_0^{2\pi} \frac{d\varphi / \sqrt{1 + \kappa \sin^2 \varphi}}{\sigma \frac{j_a}{j_W} - \eta \frac{\pi H_b^0}{H_K} \cos \varphi - \frac{\sin 2\varphi}{\sqrt{1 + \kappa \sin^2 \varphi}}}, \quad (17)$$

in which $\sigma \equiv \eta \cdot \text{sgn}(\alpha - \beta)$ and a prime in this section means quantities in current-driven case. For high-current limit, after preserving the second-order small quantities we have

$$T'_0 \approx \frac{\sigma}{\bar{\gamma} H_W^0} \frac{j_W^0}{j_a} \left\{ K_0 + \left[\frac{K_0}{2} \left(\frac{\pi H_b^0}{H_K} \right)^2 + I_1 \right] \left(\frac{j_W^0}{j_a} \right)^2 \right\}, \quad (18)$$

in which the integral $I_1(\kappa)$ is defined in Eq. (B2). Thus the time-averaged wall velocity is

$$\langle \dot{q} \rangle'_0 = -\frac{1 + \alpha\beta}{1 + \alpha^2} B_J + \frac{(\alpha - \beta) B_J}{\alpha(1 + \alpha^2)} \left[\frac{1}{2} \left(\frac{\pi H_b^0}{H_K} \right)^2 + \frac{I_1}{K_0} \right] \left(\frac{j_W^0}{j_a} \right)^2. \quad (19)$$

If we focus on the velocity dependence on j_a (thus B_J), interestingly even in the absence of bDMI, our result provides an additional $(j_a)^{-1}$ term except for the well-known first term on the right hand of Eq. (19). The appearance of bDMI strengthens this effect. On the other hand, this term helps to reorganize the $\langle \dot{q} \rangle'_0 \sim j_a$ relationship as $c'(j_a - j_a^0)/j_a + d'/j_a$, which is similar to its counterpart in field-driven case [see Eq. (10) and related discussions].

V.C $\langle \dot{q} \rangle \sim H_\perp$ dependence under large j_a

The in-plane bias field \mathbf{H}_\perp is once again turned on to manipulate chiral DWs' dynamics. Just similar to what we have discussed in Sec. IV.C, the Walker current density will inevitably be affected by \mathbf{H}_\perp , however the exact dependence is hard to obtain. Now we concentrate on the case in which the in-plane current j_a is sufficiently large that the wall already falls into the precessional-flow mode with the breathing width $\Delta = \Delta_0(1 + \kappa \sin^2 \varphi)^{-1/2}$. The period for a full circle is similar to Eq. (17) except for an additional “ $-\frac{\pi H_\perp}{H_K} \frac{\sin(\varphi - \phi_\perp)}{\sqrt{1 + \kappa \sin^2 \varphi}}$ ” term to the denominator of the integral kernel.

In the first example, we focus on longitudinal in-plane bias fields ($H_\perp = H_x$ and $\phi_\perp = 0$). Similar calculation shows that the new period is larger than T'_0 by an additional term proportional to $(j_a)^{-3}$, that is,

$$T'_x = T'_0 + \frac{\sigma I_2}{\bar{\gamma} H_W^0} \left(\frac{\pi H_x}{H_K} \right)^2 \left(\frac{j_W^0}{j_a} \right)^3, \quad (20)$$

in which the integral $I_2(\kappa)$ is defined in Eq. (B3). This leads to a new velocity

$$\langle \dot{q} \rangle'_x [H_x] = \langle \dot{q} \rangle'_0 + \frac{\alpha - \beta}{\alpha(1 + \alpha^2)} \left(\frac{\pi H_x}{H_K} \right)^2 \frac{I_2}{K_0} \left(\frac{j_W^0}{j_a} \right)^2 B_J. \quad (21)$$

For fixed H_x , the extra term in the above equation provides extra contribution to the j_a^{-1} -term in wall's velocity [see Eq. (19)]. However for fixed j_a , the $\langle \dot{q} \rangle' \sim H_x$ curve is a parabola with its center locating at $H_x = 0$ and its opening direction depends on the relative strength of α and β .

Next we turn to transverse in-plane bias fields ($H_\perp = H_y$, $\phi_\perp = \pi/2$). Similar calculation yields the large- j_a period as

$$T'_y = T'_0 + \frac{\sigma}{\bar{\gamma} H_W^0} \left[\left(\frac{\pi H_y}{H_K} \right)^2 I_3 - 2 \frac{\pi H_y}{H_K} \frac{\eta \pi H_b^0}{H_K} I_4 \right] \left(\frac{j_W^0}{j_a} \right)^3, \quad (22)$$

where the integrals $I_{3,4}(\kappa)$ have also been defined in Eq. (B3). The resulting averaged wall velocity is then

$$\langle \dot{q} \rangle'_y [H_y] = \langle \dot{q} \rangle'_0 + \frac{\alpha - \beta}{\alpha(1 + \alpha^2)} \left\{ \frac{\pi^2 I_3}{K_0} \left(\frac{H_y - \delta H'_y}{H_K} \right)^2 - \left(\frac{\pi H_b^0}{H_K} \right)^2 \frac{(I_4)^2}{K_0 I_3} \right\} \left(\frac{j_W^0}{j_a} \right)^2 B_J, \quad (23)$$

with $\delta H'_y = \eta(I_4/I_3)H_b^0$. Now the $\langle \dot{q} \rangle \sim H_y$ curve becomes a parabola with its center locating at $H_y = \delta H'_y$. Also, its opening direction has nothing to do with the wall's topological charge, but only depends on $\text{sgn}(\alpha - \beta)$. For a given magnetic heterostructure with chiral-magnet central layer, the “hard-easy ratio” κ (thus I_3, I_4) can be calculated. Similar to field-driven case, for a chiral DW with a certain wall charge η , by measuring the $\langle \dot{q} \rangle' \sim H_y$ dependence one can also extract out the bDMI strength D_b from the location of parabola center. The data from field- and current-driven cases can be cross-checked to confirm the value of bDMI strength in the underlying magnetic heterostructure.

VI. DISCUSSIONS

First of all, we want to address the feasibility of the classical Walker ansatz in Eq. (4) adopted in this work. In perfect strip-shaped heterostructures, early studies show that DMIs can induce the wall tilting χ with respect to $+\mathbf{e}_y$ [40]. However for real heterostructures with disorders, the walls take complex meandering shape with its magnetization vector rotating

several times along the wall thus show inconspicuous tilting [24, 25, 49]. This leads to negligible longitudinal component of \mathbf{H}_b which is proportional to $\nabla_y m_z$, hence explains the feasibility of using 1D Walker ansatz. Another neglected effect is the magnetization canting θ_∞ [50] in domains by in-plane fields either from intrinsic bDMI or from external exertion. When both χ and θ_∞ are considered, a more complicated wall ansatz

$$\tan \frac{\vartheta}{2} = \frac{e^R + \tan(\theta_\infty/2)}{1 + e^R \tan(\theta_\infty/2)}, \quad \phi = \varphi(t) \quad (24)$$

can be proposed with $R \equiv \eta[(x-q)\cos\chi + y\sin\chi]/\Delta$. By integrating the resulting dynamical equations over infinite strip length and finite width, the so-called “ $q - \varphi - \chi$ ”[40] or “ $q - \varphi - \chi - \Delta$ ”[51, 52] models, emerge. However they are too complicated to provide clear physical pictures in analyzing chiral wall dynamics.

Second, in steady-flow mode the wall width has explicit expression. While in precessional-flow mode the wall begins to breath, leading to a time-dependent wall width. The simple approximation in Sec. IV and V, i.e. $\Delta = \Delta_0(1 + \kappa \sin^2 \varphi)^{-1/2}$, is directly fetched from the steady-flow mode and is not the exact solution of $\Delta(t)$. However in most cases the wall does not change too much in a full circle ($|\dot{\Delta}/\Delta| \ll 1$). Therefore it can be regarded as a good approximate description of the actual wall width.

Third, under sufficiently large out-of-plane fields or in-plane currents, the chiral walls fall into the precessional-flow mode. In this work, during a full circle ($0 \leq \varphi < 2\pi$) the “Taylor expansion” method is adopted to get higher order correction (here we preserve to the second order). Also, the role of “hard-easy ratio” κ is fully revealed, especially in the center offsets of $\langle \dot{q} \rangle [H_y]$ and $\langle \dot{q} \rangle' [H_y]$ parabolas. This strategy holds under the assumption that magnetic anisotropic, in-plane bias and bDMI effective fields are all small compared with out-of-plane driving fields or in-plane currents (through j_W^0 which is proportional to H_W^0). Generally, this condition is not hard to achieve thus makes the corresponding measurements feasible. However for chiral magnets with sufficient large bDMI, to achieve the full parabola quite large driving fields or currents have to be exerted which may make the structure of chiral domain walls unstable. This possibility limits the application of our theories presented above.

Alternatively, in our recent work (see Ref. [43]) another approximation has been adopted: for large enough H_z or j_a , DWs precess almost evenly in a full circle. After linearization of trigonometric functions in dynamical equations, the average wall velocity within $\varphi \in [0, 1)$ is used to mimic the one over a full circle. Regarding this approach, we would like to present several comments: (i) The wall width is always taken as the static one, Δ_0 , which is κ -independent. This may not affect too much for wide magnetic heterostructures, however in relatively narrow ones the effects of κ could get stronger. (ii) This approach is not subject to the limitation that all other fields should be small compared with out-of-plane driving fields or in-plane currents, however it suffers from the

constraint that analytics can only hold not too far away from the dome summits or canyon bottoms. Therefore, it can not explain the further evolution of wall velocity when in-plane bias fields go faraway from the centers of domes or canyons. (iii) After series expansions, an additional absolute linear term emerges which is the direct consequence of linearization operation. For example, to compare with Eqs. (10) and (14) in the present work, the field-driven wall velocity $v_{b,T}$ in Ref. [43] can be expanded as

$$\frac{v_{b,T}}{\eta \alpha \Delta_0 \tilde{\gamma} H_z} = 1 + \frac{\pi}{4\alpha} |\Gamma| + \frac{\pi^2}{12} |\Gamma|^2, \quad (25)$$

with $\Gamma \equiv \frac{H_y}{H_z} - \eta \frac{H_b^0}{H_z} - \frac{2}{\pi} \frac{H_K}{H_z}$. Therefore the domes or canyons in Ref. [43] are generally not parabolas but cones around the dome summits or canyon bottoms. However, considering the fact that $\eta(1 + \frac{\kappa}{4})$ and I_4/I_3 approach 1 when $\kappa \rightarrow 0$ and H_K/H_z becomes neglectable for not-too-narrow geometries, the correctness of both two analytical schemes can be cross-verified.

ACKNOWLEDGMENTS

M.L. acknowledges support from the National Natural Science Foundation of China (Grant No. 11947023). B.X. is supported by the National Natural Science Foundation of China (Grant No. 11774300).

Appendix A: Maximum value and location of $|f(\varphi)|$

By setting $x \equiv \sin \varphi$ and defining

$$\mathcal{F}(x) \equiv [f(\varphi)]^2 = (1 - x^2) \left(2x + b\sqrt{1 + \kappa x^2} \right)^2, \quad (A1)$$

the searching of maximum of $|f(\varphi)|$ for $\varphi \in [0, 2\pi)$ is equivalent to the counterpart of $\mathcal{F}(x)$ for $|x| \leq 1$. We denote the location of maximum point as \tilde{x} and the corresponding maximum of $\mathcal{F}(x)$ is $\mathcal{F}(x)|_{\max} = (1 - \tilde{x}^2) \left(2\tilde{x} + b\sqrt{1 + \kappa \tilde{x}^2} \right)^2$. The resulting maximum of $|f(\varphi)|$ is thus $\sqrt{\mathcal{F}(x)|_{\max}}$ at $\sin \varphi_0 = \tilde{x}$.

Standard calculus provides us the following results:

- [a] when $0 < \kappa \leq 1$:
 (a1) for $0 < b^2 < 4/\kappa$:

$$\tilde{x} = \left[\frac{\kappa - 1}{3\kappa} + \sqrt{\frac{4(\kappa + 2)^2 - b^2\kappa(1 - \kappa)^2}{9\kappa^2(4 - b^2\kappa)}} \cdot \cos \frac{\theta + \pi}{3} \right]^{\frac{1}{2}},$$

$$\theta = \arccos \left\{ \frac{\sqrt{1 - \frac{b^2\kappa}{4}} \cdot \left[1 + \frac{b^2\kappa}{4} \left(\frac{1 - \kappa}{\kappa + 2} \right)^3 \right]}{\left[1 - \frac{b^2\kappa}{4} \left(\frac{1 - \kappa}{\kappa + 2} \right)^2 \right]^{3/2}} \right\}, \quad (A2)$$

(a2) for $b^2 = 4/\kappa$:

$$\tilde{x} = \sqrt{\frac{\kappa}{2\kappa+1}}, \quad (\text{A3})$$

(a3) for $b^2 > 4/\kappa$:

$$\begin{aligned} \tilde{x} &= \sqrt{-\frac{1-\kappa}{3\kappa} - \frac{\sqrt[3]{Y_+} + \sqrt[3]{Y_-}}{3\kappa(4-b^2\kappa)}}, \\ Y_{\pm} &= (b^2\kappa-4)^2 \left\{ \frac{(\kappa+2)^3}{2} + \frac{b^2\kappa}{8}(1-\kappa)^3 \right. \\ &\quad \left. \pm \frac{3\kappa}{2} \sqrt{\frac{3b^2[(\kappa+2)^3 + \frac{b^2}{4}(\kappa+1)(1-\kappa)^3]}{b^2\kappa-4}} \right\}, \end{aligned} \quad (\text{A4})$$

[b] when $\kappa > 1$:

(b1) for $0 < b^2 < 4/\kappa$: same as Eq. (A2),

(b2) for $b^2 = 4/\kappa$: same as Eq. (A3),

(b3) for $4/\kappa < b^2 < 4(\kappa+2)^3/[(\kappa+1)(\kappa-1)^3]$: same as Eq. (A4),

(b4) for $b^2 = 4(\kappa+2)^3/[(\kappa+1)(\kappa-1)^3]$:

$$\tilde{x} = \sqrt{\frac{\kappa^2-1}{\kappa(2\kappa+1)}}, \quad (\text{A5})$$

(b5) for $b^2 > 4(\kappa+2)^3/[(\kappa+1)(\kappa-1)^3]$:

$$\begin{aligned} \tilde{x} &= \left[\frac{\kappa-1}{3\kappa} + \sqrt{\frac{b^2\kappa(\kappa-1)^2 - 4(\kappa+2)^2}{9\kappa^2(b^2\kappa-4)}} \cdot \cos \frac{\theta}{3} \right]^{\frac{1}{2}}, \\ \theta &= \arccos \left\{ -\frac{\sqrt{1 - \frac{4}{b^2\kappa}} \cdot \left[1 - \frac{4}{b^2\kappa} \left(\frac{\kappa+2}{\kappa-1} \right)^3 \right]}{\left[1 - \frac{4}{b^2\kappa} \left(\frac{\kappa+2}{\kappa-1} \right)^2 \right]^{3/2}} \right\}. \end{aligned} \quad (\text{A6})$$

Appendix B: Definitions and values of several integrals

In this appendix, several integrals appeared in the main text are listed and calculated.

The first one is K_0 appearing in Sec. IV.B and throughout this paper:

$$K_0 = \int_0^{2\pi} \frac{d\varphi}{\sqrt{1+\kappa\sin^2\varphi}} = \frac{4}{\sqrt{1+\kappa}} K\left(\sqrt{\frac{\kappa}{1+\kappa}}\right), \quad (\text{B1})$$

in which $K(k) \equiv \int_0^{\pi/2} \frac{d\omega}{\sqrt{1-k^2\sin^2\omega}}$ is the complete elliptic integral of the first kind.

The second one is I_1 which appeared in Sec. V.B:

$$\begin{aligned} I_1 &= \int_0^{2\pi} \frac{\sin^2 2\varphi}{(1+\kappa\sin^2\varphi)^{3/2}} d\varphi \\ &= \frac{16\sqrt{1+\kappa}}{\kappa} \left[\frac{2+\kappa}{\kappa(1+\kappa)} K\left(\sqrt{\frac{\kappa}{1+\kappa}}\right) - \frac{2}{\kappa} E\left(\sqrt{\frac{\kappa}{1+\kappa}}\right) \right], \end{aligned} \quad (\text{B2})$$

in which $E(k) \equiv \int_0^{\pi/2} d\omega \sqrt{1-k^2\sin^2\omega}$ is the complete elliptic integral of the second kind.

The next three integrals are I_2 , I_3 and I_4 which appeared in Sec. V.C:

$$\begin{aligned} I_2 &= \int_0^{2\pi} \frac{\sin^2\varphi}{(1+\kappa\sin^2\varphi)^{3/2}} d\varphi \\ &= \frac{4}{\kappa\sqrt{1+\kappa}} \left[K\left(\sqrt{\frac{\kappa}{1+\kappa}}\right) - E\left(\sqrt{\frac{\kappa}{1+\kappa}}\right) \right], \\ I_3 &= \int_0^{2\pi} \frac{\cos^2\varphi}{(1+\kappa\sin^2\varphi)^{3/2}} d\varphi \\ &= \frac{4}{\kappa\sqrt{1+\kappa}} \left[(1+\kappa)E\left(\sqrt{\frac{\kappa}{1+\kappa}}\right) - K\left(\sqrt{\frac{\kappa}{1+\kappa}}\right) \right], \\ I_4 &= \int_0^{2\pi} \frac{\cos^2\varphi}{1+\kappa\sin^2\varphi} d\varphi = 2\pi \frac{\sqrt{1+\kappa}-1}{\kappa}. \end{aligned} \quad (\text{B3})$$

* lujie@yzu.edu.cn

† yjliu@yzu.edu.cn

- [1] M. Heide, G. Bihlmayer, and S. Blügel, Phys. Rev. B **78**, 140403(R) (2008).
- [2] A.Thiaville, S. Rohart, E. Jué, V. Cros, and A. Fert, Europhys. Lett. **100**, 57002 (2012).
- [3] G. Chen, J. Zhu, A. Quesada, J. Li, A. T. N'Diaye, Y. Huo, T. P. Ma, Y. Chen, H. Y. Kwon, C. Won *et al.*, Phys. Rev. Lett. **110**, 177204 (2013).
- [4] G. Chen, S. P. Kang, C. Ophus, A. T. N'Diaye, H. Y. Kwon, R. T. Qiu, C. Won, K. Liu, Y. Wu, and A. K. Schmid, Nat. Commun. **8**, 15302 (2017).
- [5] V. Risinggård and J. Linder, Phys. Rev. B **95**, 134423 (2017).
- [6] M. Li, J. Wang, and J. Lu, New J. Phys. **21**, 053011 (2019).
- [7] S. Mühlbauer, B. Binz, F. Jonietz, C. Pfleiderer, A. Rosch, A. Neubauer, R. Georgii, and P. Böni, Science **323**, 915 (2009).
- [8] X. Z. Yu, Y. Onose, N. Kanazawa, J. H. Park, J. H. Han, Y. Matsui, N. Nagaosa, and Y. Tokura, Nature **465**, 901 (2010).
- [9] W. Jiang, G. Chen, K. Liu, J. Zang, S. G. te Velthuis, and A. Hoffmann, Phys. Rep. **704**, 1 (2017).
- [10] J. S. Chen, L. J. Wang, M. Zhang, L. Zhou, R. N. Zhang, L. P. Jin, X. S. Wang, H. L. Qin, Y. Qiu, J. W. Mei *et al.*, Nano Lett. **19**, 6144 (2019).
- [11] X. Zhang, Y. Zhou, K. M. Song, T.-E. Park, J. Xia, M. Ezawa, X. Liu, W. Zhao, G. Zhao, and S. Woo, J. Phys. Condens. Matter **32**, 143001 (2020).
- [12] M. Ezawa, Phys. Rev. B **83**, 100408 (2011).
- [13] S.-Z. Lin, A. Saxena, and C. D. Batista, Phys. Rev. B **91**, 224407 (2015).
- [14] B. Göbel, A. Mook, J. Henk, I. Mertig, and O. A. Tretiakov, Phys. Rev. B **99**, 060407(R) (2019).
- [15] L. Shen, J. Xia, X. Zhang, M. Ezawa, O. A. Tretiakov, X. Liu, G. Zhao, and Y. Zhou, Phys. Rev. Lett. **124**, 037202 (2020).
- [16] X. Zhang, J. Xia, L. Shen, M. Ezawa, O. A. Tretiakov, G. Zhao, X. Liu, and Y. Zhou, Phys. Rev. B **101**, 144435 (2020).
- [17] I.Dzyaloshinsky, J. Phys. Chem. Solids **4**, 241 (1958).
- [18] T. Moriya, Phys. Rev. **120**, 91 (1960).
- [19] M. Bode, M. Heide, K. von Bergmann, P. Ferriani, S. Heinze, G. Bihlmayer, A. Kubetzka, O. Pietzsch, S. Blügel, and R. Wiesendanger, Nature **447**, 190 (2007).

- [20] S. X. Huang and C. L. Chien, *Phys. Rev. Lett.* **108**, 267201 (2012).
- [21] O. Meshcheriakova, S. Chadov, A. K. Nayak, U. K. Rößler, J. Kübler, G. André, A. A. Tsirlin, J. Kiss, S. Hausdorf, A. Kalache *et al.*, *Phys. Rev. Lett.* **113**, 087203 (2014).
- [22] S. Singh, S. W. D'Souza, J. Nayak, E. Suard, L. Chapon, A. Senyshyn, V. Petricek, Y. Skourski, M. Nicklas, C. Felser *et al.*, *Nat. Commun.* **7**, 12671 (2016).
- [23] M. Vaňatka, J.-C. Rojas-Sánchez, J. Vogel, M. Bonfim, M. Belmeguenai, Y. Roussigné, A. Stashkevich, A. Thiaville, and S. Pizzini, *J. Phys.: Condens. Matter* **27**, 326002 (2015).
- [24] E. Jué, A. Thiaville, S. Pizzini, J. Miltat, J. Sampaio, L. D. Buda-Prejbeanu, S. Rohart, J. Vogel, M. Bonfim, O. Boulle *et al.*, *Phys. Rev. B* **93**, 014403 (2016).
- [25] T. H. Pham, J. Vogel, J. Sampaio, M. Vaňatka, J.-C. Rojas-Sánchez, M. Bonfim, D. S. Chaves, F. Choueikani, P. Ohresser, E. Otero *et al.*, *Europhys. Lett.* **113**, 67001 (2016).
- [26] F. Ajejas, V. Křížáková, D. de Souza Chaves, J. Vogel, P. Perna, R. Guerrero, A. Gudin, J. Camarero, and S. Pizzini, *Appl. Phys. Lett.* **111**, 202402 (2017).
- [27] D. S. Chaves, F. Ajejas, V. Křížáková, J. Vogel, and S. Pizzini, *Phys. Rev. B* **99**, 144404 (2019).
- [28] Y. H. Choi, Y. Yoshimura, K.-J. Kim, K. Lee, T. W. Kim, T. Ono, C.-Y. You, and M. H. Jung, *Sci. Rep.* **6**, 23933 (2016).
- [29] F. Ajejas, A. Gudin, R. Guerrero, A. A. Barcelona, J. M. Diez, L. de Melo Costa, P. Olleros, M. A. Niño, S. Pizzini, J. Vogel *et al.*, *Nano Lett.* **18**, 5364 (2018).
- [30] A. Hrabec, V. Křížáková, S. Pizzini, J. Sampaio, A. Thiaville, S. Rohart, and J. Vogel, *Phys. Rev. Lett.* **120**, 227204 (2018).
- [31] T. Dohi, S. DuttaGupta, S. Fukami, and H. Ohno, *Appl. Phys. Lett.* **114**, 042405 (2019).
- [32] D.-H. Kim, D.-Y. Kim, S.-C. Yoo, B.-C. Min, and S.-B. Choe, *Phys. Rev. B* **99**, 134401 (2019).
- [33] S. DuttaGupta, S. Fukami, C. Zhang, H. Sato, M. Yamanouchi, F. Matsukura, and H. Ohno, *Nat. Phys.* **12**, 333 (2016).
- [34] P. C. Filippou, J. Jeong, Y. Ferrante, S.-H. Yang, T. Topuria, M. G. Samant, and S. S. P. Parkin, *Nat. Commun.* **9**, 4653 (2018).
- [35] G. V. Karnad, F. Freimuth, E. Martinez, R. Lo Conte, G. Gubbiotti, T. Schulz, S. Senz, B. Ocker, Y. Mokrousov, and M. Kläui, *Phys. Rev. Lett.* **121**, 147203 (2018).
- [36] A. Hrabec, K. Shahbazi, T. A. Moore, E. Martinez, and C. H. Marrows, *Nanotechnology* **30**, 234003 (2019).
- [37] D. Lau and V. Sokalski, *AIP Advances* **9**, 035208 (2019).
- [38] P.-B. He, M.-Q. Cai, and Z.-D. Li, *Phys. Rev. B* **102**, 224419 (2020).
- [39] P. Bak and M. H. Jensen, *J. Phys. C: Solid State Phys.* **13**, L881 (1980).
- [40] O. Boulle, S. Rohart, L. D. Buda-Prejbeanu, E. Jué, I. M. Miron, S. Pizzini, J. Vogel, G. Gaudin, and A. Thiaville, *Phys. Rev. Lett.* **111**, 217203 (2013).
- [41] P.-B. He, *Eur. Phys. J. B* **86**, 412 (2013).
- [42] M. Li, Z. An, and J. Lu, *Phys. Rev. B* **100**, 064406 (2019).
- [43] J. Lu, M. Li, and X. R. Wang, *Phys. Rev. B* **101**, 134431 (2020).
- [44] M. Li and J. Lu, *J. Magn. Magn. Mater.* **525**, 167684 (2021).
- [45] J. Du, M. Li, and J. Lu, *Phys. Rev. B* **103**, 144429 (2021).
- [46] J.C. Slonczewski, *A.I.P. Conf. Proc.* **5**, 170 (1972).
- [47] A. Thiaville, Y. Nakatani, J. Miltat, Y. Suzuki, *Europhys. Lett.* **69**, 990 (2005).
- [48] X. R. Wang, P. Yan, and J. Lu, *Europhys. Lett.* **86**, 67001 (2009).
- [49] K. Shahbazi, A. Hrabec, S. Moretti, M. B. Ward, T. A. Moore, V. Jeudy, E. Martinez, and C. H. Marrows, *Phys. Rev. B* **98**, 214413 (2018).
- [50] J. Lu, *Phys. Rev. B* **93**, 224406 (2016).
- [51] S. A. Nasser, S. Moretti, E. Martinez, C. Serpico, and G. Durin, *J. Magn. Magn. Mater.* **426**, 195 (2017).
- [52] S. A. Nasser, E. Martinez, and G. Durin, *J. Magn. Magn. Mater.* **468**, 25 (2018).